

Article

# Simulation of Real Defect Geometry and Its Detection Using Passive Magnetic Inspection (PMI) Method

Milad Mosharafi <sup>1,\*</sup>, SeyedBijan Mahbaz <sup>2</sup> and Maurice B. Dusseault <sup>2</sup>

<sup>1</sup> Mechanical and Mechatronics Engineering Department, University of Waterloo, Ontario, N2L 3G1, Canada

<sup>2</sup> Earth and Environmental Sciences Department, University of Waterloo, Ontario, N2L 3G1, Canada; smahbaz@uwaterloo.ca (S.M.); mauriced@uwaterloo.ca (M.B.D.)

\* Correspondence: mmoshara@uwaterloo.ca; Tel.: +1-519-504-3499

Received: 26 May 2018; Accepted: 4 July 2018; Published: 14 July 2018



**Abstract:** Reinforced concrete is the most commonly used material in urban, road, and industrial structures. Quantifying the condition of the reinforcing steel can help manage the human and financial risks that arise from unexpected reinforced concrete structure functional failure. Also, a quantitative time history of reinforcing steel condition can be used to make decisions on rehabilitation, decommissioning, or replacement. The self-magnetic behavior of ferromagnetic materials is useful for quantitative condition assessment. In this study, a ferromagnetic rebar with artificial defects was scanned by a three-dimensional (3D) laser scanner. The obtained point cloud was imported as a real geometry to a finite element software platform; its self-magnetic behavior was then simulated under the influence of Earth's magnetic field. The various passive magnetic parameters that can be measured were reviewed for different conditions. Statistical studies showed that 0.76% of the simulation-obtained data of the rebar surface was related to the defect locations. Additionally, acceptable coincidences were confirmed between the magnetic properties from numerical simulation and from experimental outputs, most noticeably at hole locations.

**Keywords:** reinforce concrete; rebar; defect; self-magnetic behavior; magnetic flux density; probability paper method; Passive Magnetic Inspection (PMI)

## 1. Introduction

Reinforced concrete as a composite infrastructure material is widely used in construction because of its excellent properties [1] and construction ease. Three factors control the behavioral responses of reinforced concrete: the reinforcing steel (generically referred to as rebar in this article), which has a noticeable ductile nature; the concrete itself, which has a noticeable brittle nature (low tensile strength but high compressive strength); and the condition of the rebar–concrete bonding (to achieve reliable stress transfer) [2].

Reinforced concrete is commonly used in infrastructure such as buildings, bridges, and highway construction [3]. The quality of a country's transportation system is mostly based on the conditions of its highway bridges, all of which contain steel. At the present time, apparently, approximately 28% of concrete bridge decks in the United States (US) and 33% of highway bridges in Canada can actually be considered operationally deficient or in a condition warranting the cessation of active service, mainly because of rebar corrosion [4].

Rebar corrosion is common in environmentally-exposed structures; it reduces the service life of these structures and impacts load-carrying capacity [5]. In the worst cases, structural failure occurs because corrosion reduces a stressed rebar's cross-sectional area [6] to the point of rupture. Rebar corrosion also degrades the bonding quality and can create cracks in the structure from

volumetric expansion [7,8]. Bond deterioration leaves structures more vulnerable to vibrations related to daily usage or earthquakes [9].

The corrosion of steel rebar embedded in concrete falls into two categories: one is related to the specifications of the rebar and the concrete; the other includes the environmental conditions (temperature, humidity, pH, salinity, etc.) to which the structure is exposed [10]. Exposure to chloride ions, usually mostly from environmental exposure, is the most significant reason for rebar corrosion [11]. Long-term exposure to chloride ions deteriorates the passive layer of oxide on the steel rebar, eventually causing significant deterioration or structural failure, which can carry substantial economic loss [10]. To reduce safety threats and financial impact, corrosion-threatened rebar condition should be monitored so that risks can be quantitatively managed (repair, replace, restore) [12].

The visual inspection method (VI) is commonly used to assess the conditions of reinforced structures [13]. VI evaluates the external surface of the structure without directly assessing the internal conditions [14]. Even with detailed rubrics and photo imagery, VI methods are weak and semi-quantitative at best, and they must be done in conjunction with other non-destructive methods [15]. Reinforced concrete can be inspected for different types of defects using various types of non-destructive testing (NDT) methods [16]; the most common methods are potential measurement survey [17], galvanic current measurement [18], ground penetrating radar (GPR) [19], rebound hammer [20], ultrasonic [21], and radiography [22].

Each NDT method has limitations [23]; for instance, the macro-current measurement is complicated to interpret, since its results are influenced by the distance between anode and cathode and humidity [24]. GPR results are influenced by the existence of voids and variable internal moisture conditions [25], which can confound interpretations in many ways, such as confusion with background structures, shadowing, or false identification of gaps or previously repaired sites as being corrosion sites (Type I errors) [4]. Half-cell potential surveys can only mark corrosion locations; they give no information about the corrosion extent [26]. Ultrasonic pulse velocity (UPV) or Schmidt hammer techniques assess the mechanical properties of concrete with no information directly related to rebar corrosion [27]. Similarly, radiographic and acoustic inspections can assess concrete conditions, but give no direct information related to rebar conditions [28].

Some active magnetic-based methods such as magnetic flux leakage (MFL) can provide information directly related to the rebar corrosion condition [29]. Such methods need an external source such as electromagnets to properly magnetize objects during inspection [30], which increases assessment time and energy costs. These methods are challenging to perform on structures with complicated geometries [31], and complex rebar geometries can hamper clear interpretation of different data sets collected over time.

With the intent of providing a better measure that is quantitative and consistent, we introduce the passive magnetic method, which takes advantage of the Earth's natural magnetic field in order to inspect ferromagnetic structures [32]. Passive magnetic methods require no special preparation [33] or artificial magnetic source [34], and use anomalies in the passive magnetic flux density to locate defects [35]. This method can detect rebar defects such as corrosion sites or cracks [33], and stress changes that impact the crystalline ferromagnetic structure [36].

We built a Passive Magnetic Inspection (PMI) tool to exploit the passive magnetic concept and examine the corrosion condition of embedded rebar by scanning from the external concrete surface [8]. Preliminary successes have been described [37] in which solid rebar was sketched in COMSOL<sup>R</sup> software version 5.3a (COMSOL Group, Stockholm, Sweden). based on a real rebar's geometry. It was then magnetized, assuming a certain value of magnetic field. Next, the passive magnetic behavior was investigated at a fixed distance from the rebar. Building on that work, in this current paper, the same ferromagnetic steel rebar with artificial defects is scanned with a three-dimensional (3D) laser scanner to generate a detailed point cloud of the structure. This point cloud then serves as the geometry basis for the finite element method software (COMSOL<sup>R</sup> software), in studying how the Earth's magnetic field affects the rebar. Different magnetic properties of the object are extracted and

interpreted at several distances from the rebar, and the parameters influencing them are investigated. Additionally, a statistical detection method is presented as a new development in passive magnetic data processing and interpretation.

## 2. Theoretical Background and Methodology

The Earth's internal magnetic field is caused by liquid iron motions in the planetary core [38,39], plus contributions from other sources such as mantle movements, the nature of the lithosphere, etc. [40]. The magnetic field is a three-dimensional vector [41] with a harmonic pattern due to the globe's rotational movement [42]. The vector originates from the surface of the Earth and extends beyond the atmosphere, and its magnitude and orientation are functions of location [41] and time [40].

Natural magnetic fields and other influential local magnetic sources [37], combined with internal and external stresses, can change the scattered stray magnetic field of ferromagnetic materials [43]. Internal domain walls' displacement and magnetic-moment rotation in ferromagnetic materials happen under the influence of external magnetic fields [44], and there are relationships between the micro-magnetic characteristics of these materials and their mechanical responses [45]. For example, if the steel is deformed significantly in the presence of a magnetic field, the magnetization of the domains and their orientation within the steel are affected.

Self-magnetic flux leakage (SMFL) is assumed to take place in the stress concentration areas of ferromagnetic materials affected by mechanical load under the Earth's magnetic field [46], and this condition can remain even after removing the load, creating detectable magnetic leakage at the material surface [47]. Measuring SMFL at the surface of the materials helps in estimating their stress-strain states (SSSs), which is an important parameter in determining a structure's reliability [48]. Therefore, the relation between localized stress and oriented magnetic domains is useful for detecting defects in ferromagnetic materials within the background magnetic field of the Earth [49].

Magnetic field parameters at a point in space are represented by magnetic flux density (B) and an external magnetic field (H). B and H are vectors with a proportional magnitude and parallel directions. Magnetic flux density (B) represents the closeness of the magnetic field lines, and shows the strength of the magnetic field [50]. Also, Gauss's magnetic field law states that  $\nabla \cdot \mathbf{B} = 0$  [51]. H and B may have a complex relationship in magnetic materials [52], but engineers usually invoke the relation established by Faraday and Maxwell, which demonstrates that B is produced in a magnetizable material due to the existence of a primary magnetic field (H) [53].

Numerical simulation of the PMI method is performed based on the stray magnetic field ( $H_d$ ) and the stray magnetic field energy ( $E_d$ ) [37]. Hubert and Schäfer in 1998 [54] presented the relation for calculating the stray magnetic field (Equation (1)), based on summarizing Gauss's magnetic field law. In Equation (1), magnetic polarization (J) is the product of "volume-normalized magnetization" M, multiplied by "vacuum magnetic permeability of free space"  $\mu_0$ . Additionally, a relation suggested for estimating the stray magnetic field energy uses the balance of the magnetic charges as well as their integration over the volume of the ferromagnetic material (Equation (2)).

$$\operatorname{div} H_d = -\operatorname{div} \left( \frac{J}{\mu_0} \right) \quad (1)$$

$$E_d = \frac{1}{2} \mu_0 \int_{\text{all space}} H_d^2 dV = -\frac{1}{2} \mu_0 \int_{\text{sample}} H_d \cdot J dV \quad (2)$$

Based on potential theory, volume charge density ( $\lambda_V$ )—Equation (3)—and surface charge density ( $\sigma_S$ )—equations (4) and (5)—are other parameters related to magnetization (M)—Equation (6)—and can be implemented for computing stray fields. Surface charge density is calculated by Equation (4) when there is just one magnetic medium; Equation (5) is applied when there are two varied different

media with their own magnetization values and a specific vector perpendicular to the separation plane of those materials ( $n$ ):

$$\lambda_V = -\text{div}M \tag{3}$$

$$\sigma_S = M \cdot n \tag{4}$$

$$\sigma_S = (M_1 - M_2) \cdot n \tag{5}$$

$$M(r) = J(r) / J_s \tag{6}$$

According to Equation (7), the stray field energy at a position ( $r$ ) can be also calculated through the negative gradient of the potential of the stray field energy at a place ( $\Phi_d(r)$ ) [55], where  $\Phi_d(r)$ —Equation (8)—is a function of magnetization saturation ( $J_s$ ), volume charge density ( $\lambda_V$ ), surface charge density ( $\sigma_S$ ), and the derivative of the position vector ( $r'$ ). Next, the magnetic field energy is obtained from Equation (9) through the integration functions of surface charge density and volume charge density over the volume and surface, respectively.

$$H_d(r) = -\text{grad}\Phi_d(r) \tag{7}$$

$$\Phi_d(r) = \frac{J_s}{4\pi\mu_0} \left[ \int \frac{\lambda_V(r')}{|r-r'|} dV' + \int \frac{\sigma_S(r')}{|r-r'|} dS' \right] \tag{8}$$

$$E_d = J_s \left[ \int \lambda_V(r)\Phi_d(r)dV + \int \sigma_S(r)\Phi_d(r)dS \right] \tag{9}$$

For conducting this research article, we scanned 373.87 mm of the surface of a ferromagnetic rebar (low-carbon steel), with a diameter of 16 mm, and two artificial defects (Table 1) [37], using a high-resolution 3D laser scanner (Figure 1a) [56]. The shape of the rebar was created with cloud points (Figure 1b) that were modified and converted to a mesh by Mesh Lab V1.3.2 (<http://meshlab.sourceforge.net/>). Subsequently, the produced mesh was imported to COMSOL<sup>R</sup> software and converted to a discretized surface and solid, respectively (Figure 1c). The solid rebar was simulated via COMSOL<sup>R</sup> software with regard to the magnetic field of the Earth, different components of magnetic flux density were investigated at different spacing, related simulation results were compared with our previous experimental results, and statistical approaches were introduced.

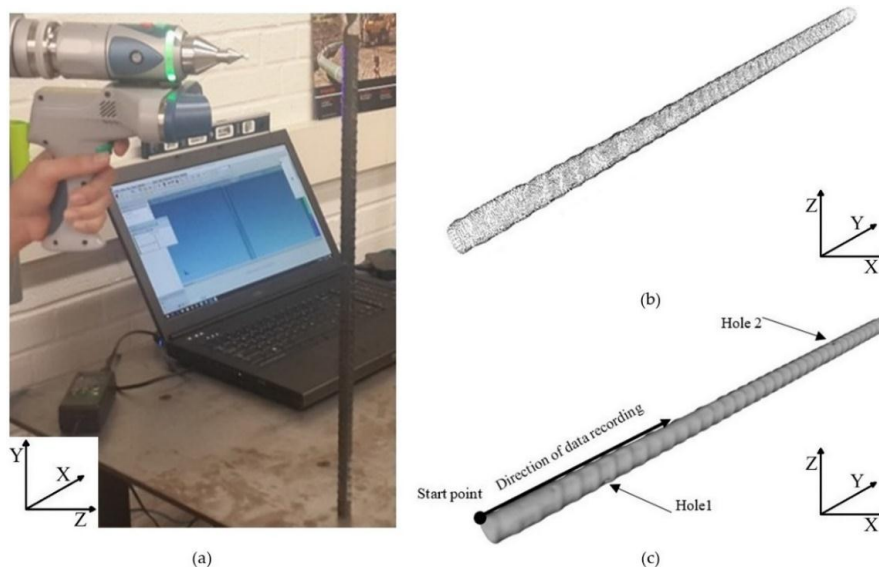


**Figure 1.** Process of converting the rebar geometry to a solid model: (a) scanning the rebar with three-dimensional (3D) laser scanner; (b) cloud points of rebar, presented in MeshLab; (c) solid illustration of rebar.

**Table 1.** Specifications of the two holes in the rebar.

| Hole Name | Diameter (mm) | Depth (mm) | Y-Location from the Rebar's Start Point (mm) |
|-----------|---------------|------------|--|
| Hole 1    | 0.58          | 1.24       | 57.91  |
| Hole 2    | 0.68          | 0.57       | 282.67                                       |

### 3. Simulations and Results

After converting the rebar mesh to solid in COMSOL<sup>R</sup> software, the magnetic behavior simulation was undertaken. Considering the variations of Earth's magnetic field in time and location, to obtain consistent and realistic results the average (within a year) of the different components of the magnetic field for the Waterloo, Ontario region (the location of the experiments) was adopted for the simulations (Table 2). Moreover, since the unitless relative magnetic permeability of low-carbon steels (ASTM 1020) range from 50 to 100 [57,58], a relative magnetic permeability of 75 was selected for this study.

**Table 2.** Background magnetic field (magnetic field of the Earth): from August 2016 to August 2017 (Adapted from Natural Resources Canada (<http://www.nrcan.gc.ca>)).

| Background Magnetic Field (X-Component) | Background Magnetic Field (Y-Component) | Background Magnetic Field (Z-Component) |
|---|---|---|
| 18 $\mu$ T                              | −3 $\mu$ T                              | 50 $\mu$ T                              |

The duration of exposure to an external magnetic field will affect the magnetic behavior of ferromagnetic materials. In reality, ferromagnetic materials are affected by the magnetic field of the Earth from the beginning of their production process. There may also be some unknown external magnetic sources in the surrounding environment that affect the magnetic behavior of ferromagnetic objects [59]. However, as accurately as possible, we can apply the magnetic field of the Earth to the object and simulate its magnetic behavior, although some divergence will exist between the simulation and the experimental results.

To consider the Earth's magnetic field in the simulation, the rebar was located in a regular space (Figure 2) with dimensions of 100 mm  $\times$  150 mm  $\times$  410 mm, which included the magnetic field presented in Table 2 and Figure 3. To have better control of simulation parameters, the box and rebar were meshed separately with tetrahedral meshes according to the specifications in Table 3 (Figure 4a,b). Then, the rebar and box were jointly subjected to the simulation process as a single system (Figure 4c). The values of the different components (X, Y, and Z) of the magnetic flux densities were recorded for the Y direction of the rebar (i.e., the path parallel to the rebar's length). This path is at the surface of the rebar, and extends from one side (Edge A) to the other side of the box (Edge B) (Figure 5).

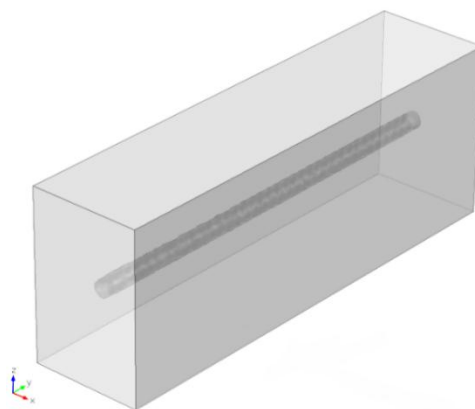


**Figure 2.** Solid rebar located in a box.

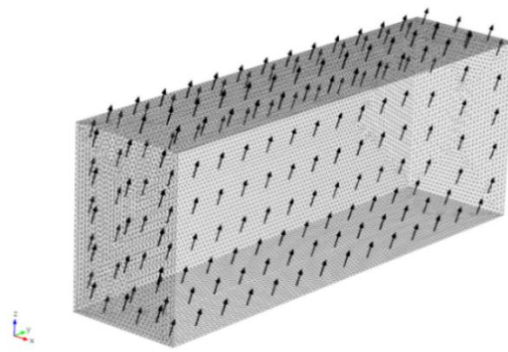


**Figure 3.** Box used in analysis; arrows show the resultant vector for X, Y, and Z components of Earth’s magnetic field.

**Table 3.** Mesh specifications of rebar and box in the initial simulation.

| Section Name                            | Rebar   | Box  |
|---|---------|------|
| Maximum element size (mm)               | 2       | 8    |
| Minimum element size (mm)               | 1       | 4.1  |
| Maximum element growth rate             | 1.45    | 1.45 |
| Curvature factor                        | 0.5     | 0.5  |
| Resolution of narrow regions            | 0.6     | 0.6  |
| Number of degrees of freedom (in total) | 601,773 |      |

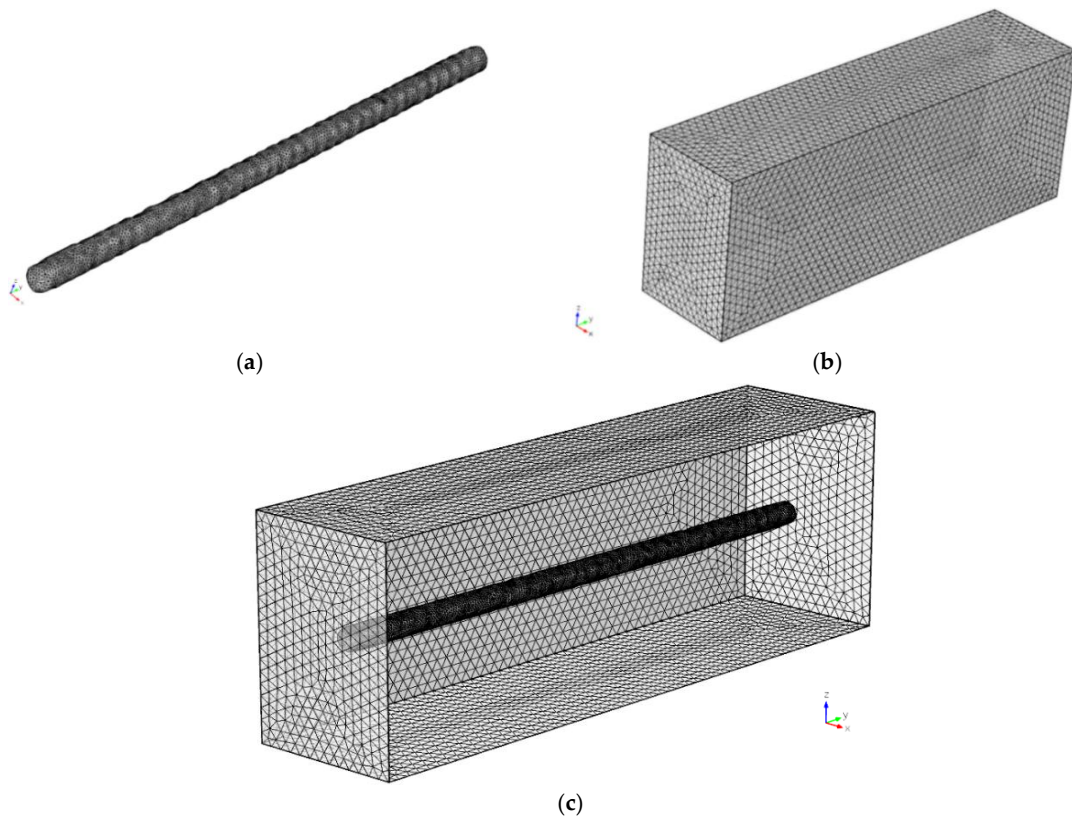


**Figure 4.** Initial meshes of the system: (a) rebar mesh with its initial sizes; (b) box mesh with its initial sizes; (c) rebar and box meshes as a single system (front face of the box is removed for better visualization).

As observed in Figure 6, at first, the values of all of the components of magnetic flux densities are equal to the background magnetic flux (the magnetic field of the Earth). When the Y distance reaches

about 18.065 mm, at the end of the rebar, the values of all of the components begin to reflect the impact of the magnetic properties of the ferromagnetic rebar on the magnetic fluxes.

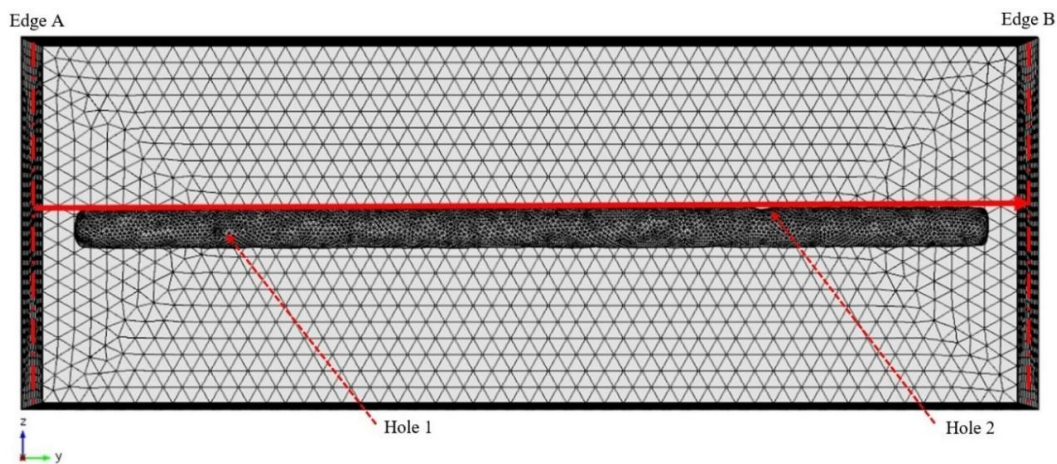


Figure 5. Path of the data recording (at the surface of the rebar in the Y direction).

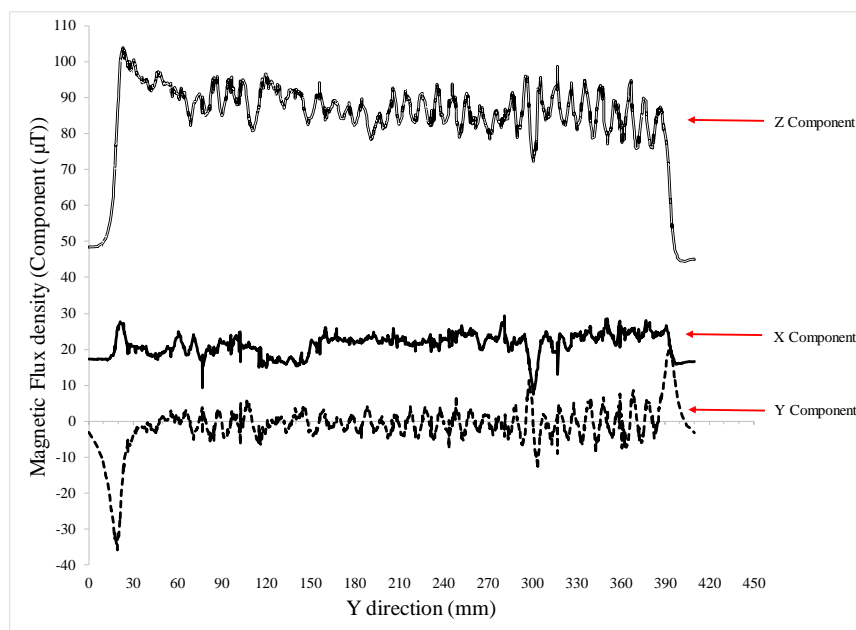


Figure 6. Values of different components (X, Y and Z) of the magnetic flux densities in the Y direction at the surface of the rebar (initial mesh of the rebar and box).

The values of all of the components have a harmonic variation because of the corrugated rebar shape. When the Y distance reaches the end of the rebar, all of the components of magnetic flux densities revert to the magnitudes of the background magnetic field. However, there is a distinguishable irregularity in the direction and values of all of the components at the location of Hole 2 (~301 mm from Edge A of the box). This irregularity is in the form of a minimum peak in the values of the Z and X magnetic flux densities, and in the form of a sudden change in the gradient of the Y-component of the magnetic flux density (a spike above the zero line, followed by a sudden dip below the zero line, then a sharp jump back to the zero line).

There are some outlier values in the different components of magnetic flux densities, which are related to the specifications of the elements used in this simulation. In order to have mesh element independent results, more accurate element specifications are implemented (Table 4). Then, the maximum

and minimum values of the Z-component magnetic flux density (as a representative metric) from 295.0592 mm to 307.0592 mm (values symmetric about the fixed extent of Hole 2) are extracted. The location of Hole 2 was chosen because of its importance in our investigation. The differences between the maximum and minimum of these values are also used to verify the convergence of the simulation outcomes.

The values of the maximum and minimum magnetic flux densities become stable at mesh numbers 4 and 8 (Table 4), respectively (Figures 7 and 8). The difference between the maximum and minimum magnetic flux densities in the Z-component stabilize at rebar mesh #5 (Figure 9). Hence, the result of mesh #8 is used for continuing the simulation. The magnetic flux density values for mesh #8 have no out-of-range or disorder trend, compared with the trend of rebar mesh #1, which was the initial simulation (Figure 10).

**Table 4.** Different mesh specifications of rebar, with the fixed mesh specifications of box mesh as #1.

| Mesh | Maximum Element Size (mm) | Minimum Element Size (mm) | Maximum Element Growth Rate | Curvature Factor | Resolution of Narrow Regions | Number of Degrees of Freedom (in Total) |
|------|---------------------------|---------------------------|-----------------------------|------------------|------------------------------|---|
| 1    | 2.000                     | 1.000                     | 1.450                       | 0.500            | 0.600                        | 601,773                                 |
| 2    | 1.340                     | 0.670                     | 1.407                       | 0.450            | 0.636                        | 1,267,526                               |
| 3    | 0.898                     | 0.449                     | 1.364                       | 0.405            | 0.674                        | 3,324,359                               |
| 4    | 0.602                     | 0.301                     | 1.323                       | 0.365            | 0.715                        | 9,764,894                               |
| 5    | 0.571                     | 0.286                     | 1.310                       | 0.361            | 0.722                        | 10,441,703                              |
| 6    | 0.5605                    | 0.278                     | 1.295                       | 0.3505           | 0.746                        | 10,995,911                              |
| 7    | 0.550                     | 0.270                     | 1.280                       | 0.340            | 0.770                        | 11,594,725                              |
| 8    | 0.530                     | 0.240                     | 1.260                       | 0.330            | 0.780                        | 12,877,797                              |
| 9    | 0.500                     | 0.200                     | 1.250                       | 0.320            | 0.790                        | 15,173,763                              |
| 10   | 0.460                     | 0.160                     | 1.220                       | 0.280            | 0.810                        | 19,243,609                              |
| 11   | 0.446                     | 0.141                     | 1.100                       | 0.240            | 0.830                        | 20,879,674                              |

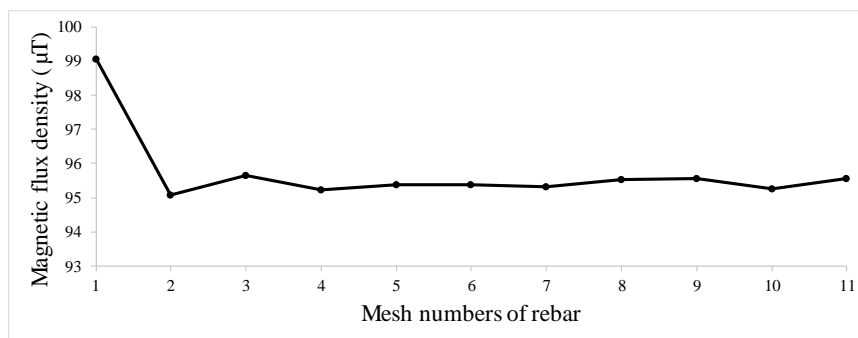


**Figure 7.** Maximum values of Z-component magnetic flux density, from 295.0592 mm to 307.0592 mm (values related to Hole 2), for different mesh specifications of rebar with fixed box mesh #1.

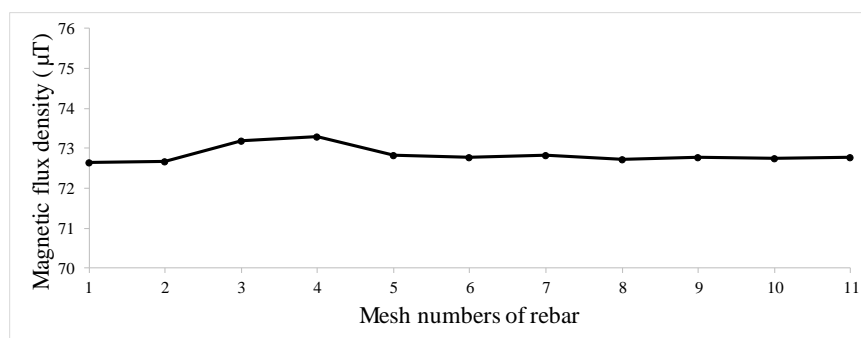


**Figure 8.** Minimum values of Z-component magnetic flux density, from 295.0592 mm to 307.0592 mm (values related to Hole 2), for different mesh specifications of rebar with fixed box mesh #1.

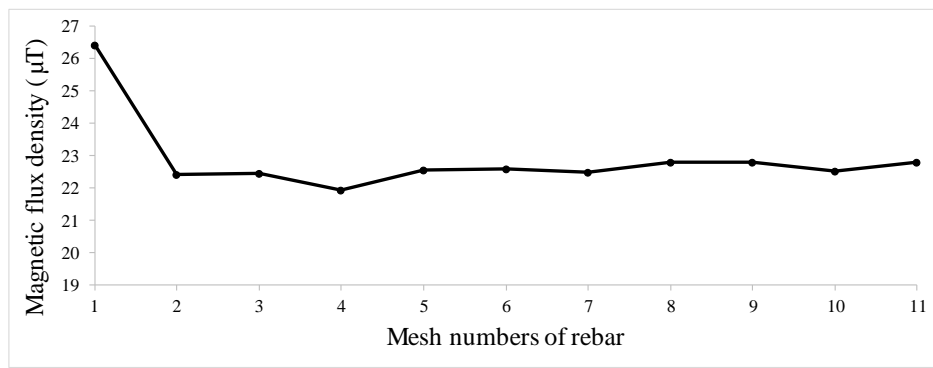


**Figure 9.** Difference between the maximum and minimum values of Z-component magnetic flux density, from 295.0592 mm to 307.0592 mm (values related to Hole 2), for different mesh specifications of rebar with fixed box mesh #1.

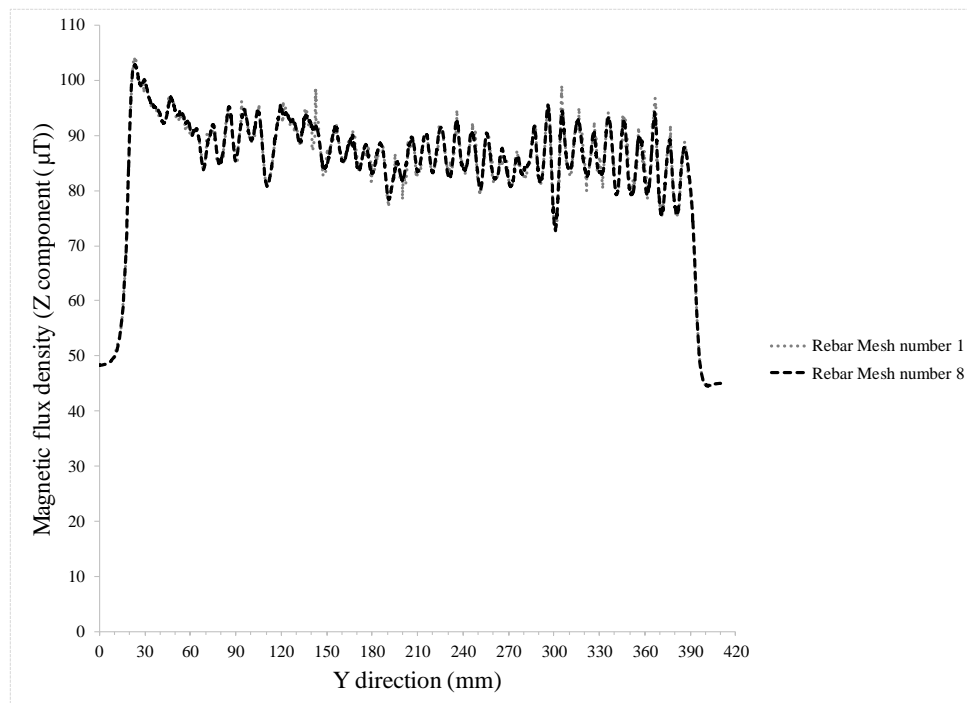


**Figure 10.** Comparison between the values of Z-component magnetic flux density of rebar mesh #8 and rebar mesh #1, with fixed box mesh (box mesh #1).

To determine the effect of spacing, values of the magnetic flux density (rebar mesh #8) with different spacing were investigated. It was understood that increasing the spacing between the rebar and the recording point would result in some outliers in the trend of the Z-component magnetic flux density, related to the specifications of the tetrahedral elements used in the box. To make the results of the simulation independent of the element specifications, more accurate element specifications were applied to the box (Table 5). As a representative result, the magnetic flux densities for the Z-component at a distance of 16 mm were extracted (Figure 11). The maximum and minimum values from 295.0592 mm to 307.0592 mm (values related to Hole 2) were reviewed. Subsequently, the difference between the maximum and minimum values was investigated, and we found that the values became stable with box mesh #5 (Figures 12–14).

**Table 5.** Different mesh specifications of box, with the fixed mesh specifications of rebar (rebar mesh #8).

| Mesh | Maximum Element Size (mm) | Minimum Element Size (mm) | Maximum Element Growth Rate | Curvature Factor | Resolution of Narrow Regions | Number of Degrees of Freedom (in Total) |
|------|---------------------------|---------------------------|-----------------------------|------------------|------------------------------|---|
| 1    | 8.000                     | 4.100                     | 1.450                       | 0.500            | 0.600                        | 12,877,797                              |
| 2    | 7.720                     | 3.400                     | 1.330                       | 0.410            | 0.620                        | 13,794,957                              |
| 3    | 6.820                     | 2.300                     | 1.300                       | 0.400            | 0.650                        | 14,188,984                              |
| 4    | 5.810                     | 1.400                     | 1.250                       | 0.350            | 0.680                        | 15,058,001                              |
| 5    | 4.110                     | 1.100                     | 1.190                       | 0.290            | 0.710                        | 17,446,126                              |
| 6    | 2.840                     | 0.850                     | 1.150                       | 0.250            | 0.730                        | 22,627,445                              |
| 7    | 2.250                     | 0.820                     | 1.140                       | 0.230            | 0.730                        | 28,481,960                              |
| 8    | 2.210                     | 0.815                     | 1.130                       | 0.230            | 0.740                        | 29,650,862                              |

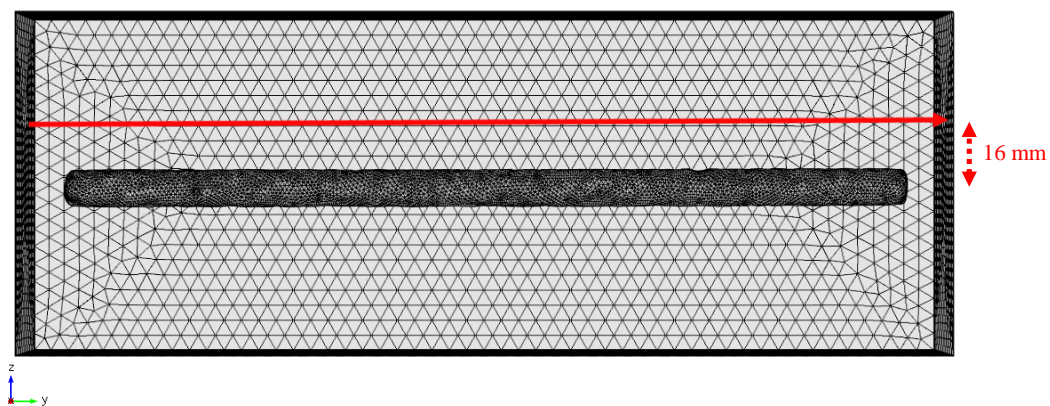


**Figure 11.** Path of data recording (with distance 16 mm from center of the rebar).

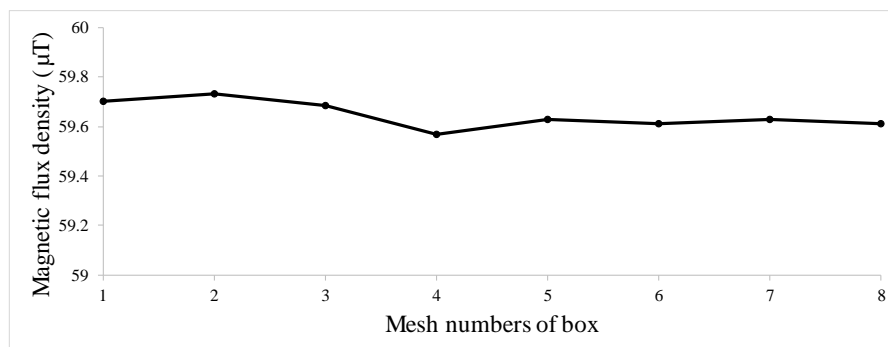


**Figure 12.** Maximum values of Z-component magnetic flux density, from 295.0592 mm to 307.0592 mm (values related to Hole 2), for different box mesh specifications with fixed rebar mesh #8 (Table 4).

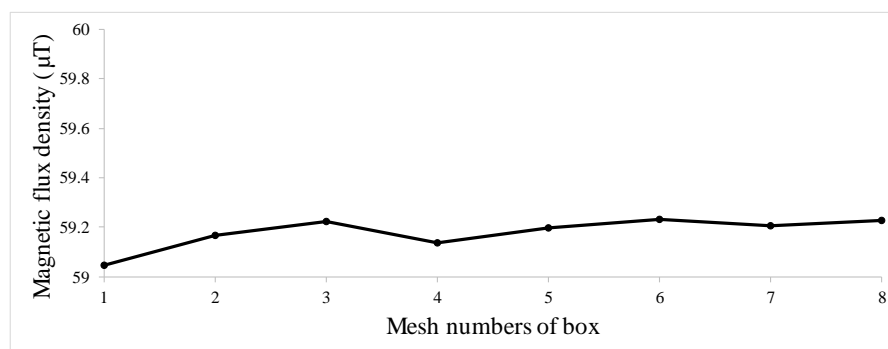


**Figure 13.** Minimum values of Z-component magnetic flux density, from 295.0592 mm to 307.0592 mm (values related to Hole 2), for different box mesh specifications with a fixed rebar mesh #8 (Table 4).

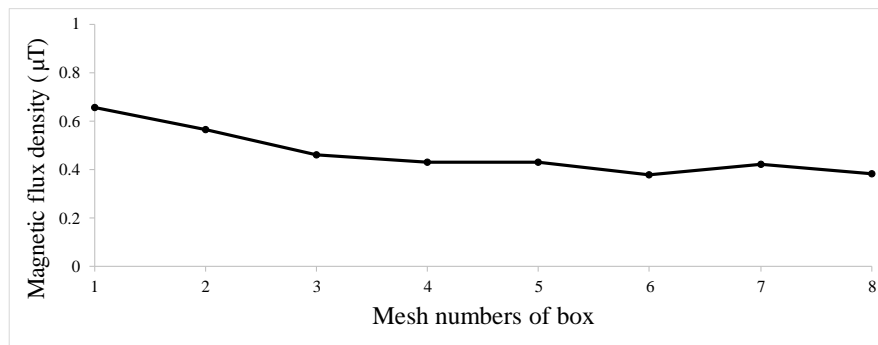


**Figure 14.** Difference between the maximum and minimum values of Z-component magnetic flux density, from 295.0592 mm to 307.0592 mm (values related to Hole 2), for different box mesh specifications with fixed rebar mesh #8 (Table 4).

According to Figures 7–9 and 12–14, the outcomes from the simulation of the rebar with mesh #8 and box mesh #5, the optimum mesh specifications, were chosen for the rest of the investigations. After the optimum mesh specifications, achieved by increasing the meshing accuracy, the biggest difference in the maximum and minimum values of magnetic flux densities (of the same place) are respectively less than 0.01 μT and 0.04 μT, which are considered negligible. Additionally, the same values are observed for the maximum and minimum values of magnetic data when the element accuracy is increased. The same magnetic values mean that the results converge and are independent of the mesh specifications.

Carrying out simulations with optimum mesh specifications led to a graphical representation (Figure 15), which shows the behavior of the Z-component magnetic flux density at the location of Hole 2. Also, a planar slice of the magnetic field under the rebar in Figure 15 shows the conditions of the stray magnetic field around the rebar. As the distance from the rebar increases, the stray magnetic field around the rebar decreases relatively uniformly and symmetrically.

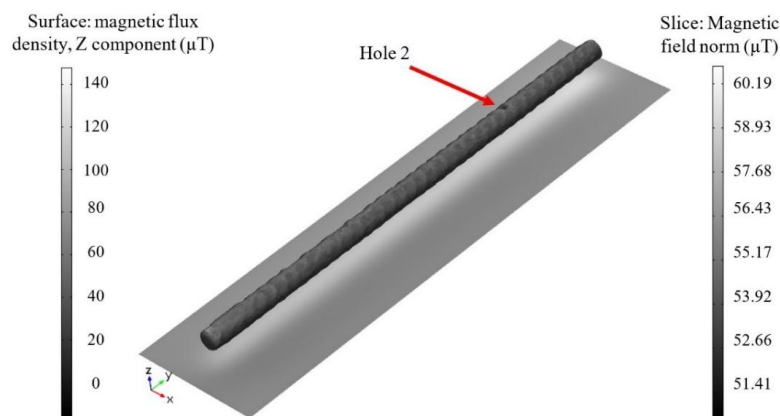


**Figure 15.** Behavior of Z-component magnetic flux density and normal magnetic field around the rebar (rebar mesh #8 and box mesh #5).

Figure 16 shows the values of magnetic flux densities of rebar with optimum mesh specifications at different spacings from the center of the rebar, ranging from 8 mm (surface level) to 72 mm (maximum distance from the surface). The behavior of the Z-component magnetic flux density is distinguishable at Hole 2 at a maximum of 16 mm from the rebar’s center (Figure 16), which is a distance equal to 8 mm from the rebar’s surface (this distance represents how thick the concrete above the bar can be for detection of the buried defects). According to the simulation results, it seems that the technique can be used only for very thin concrete layers with a maximum thickness of 8 mm.

It should be mentioned that the simulations were performed under the Earth’s present magnetic field, but ferromagnetic materials are considered saturated by the natural magnetic field, and may show stronger magnetic behavior.

For further investigation, the data-recording distance was increased to the maximum possible distance from the rebar, aligning with the inside edge of the box. At larger distances, the magnetic flux density trend becomes smoother and straighter, and approaches the background magnetic field. The minimum values of the Z-component magnetic flux density, from 295.0592 mm to 307.0592 mm (values related to Hole 2), were considered for different distances. Increasing the vertical distance (in the Z direction) of the data recording line logarithmically decreased the minimum value of the Z-component magnetic flux density until this value reached an approximately constant value. The trend line showing the relation between the minimum values of the Z-component magnetic flux density and data recorded at various distances is a fourth-order polynomial equation (Figure 17).

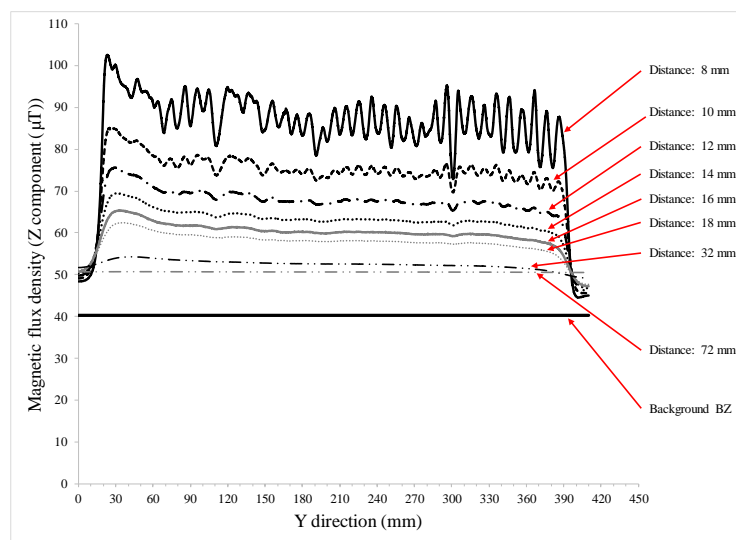


**Figure 16.** Values of magnetic flux densities of rebar mesh #8 and box mesh #5 at different vertical distances from the center of the rebar.

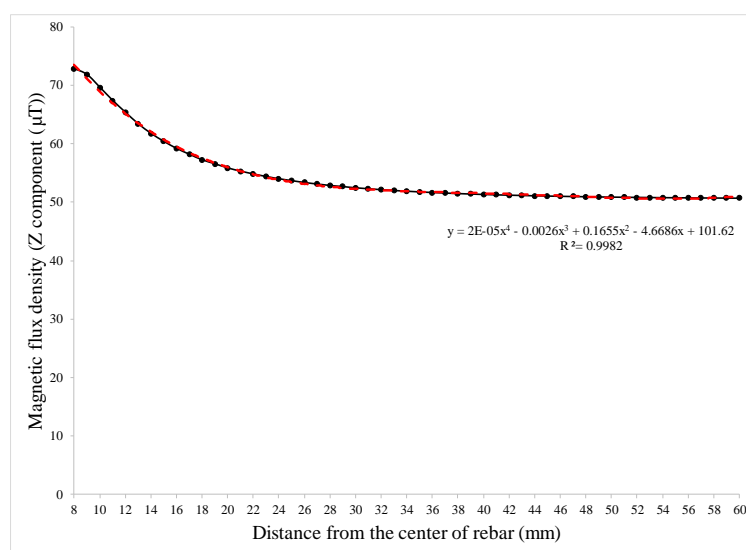


**Figure 17.** Behavior of the minimum values of the Z-component magnetic flux density, from 295.0592 mm to 307.0592 mm (values related to Hole 2), of rebar mesh #8 and box mesh #5, recorded at different vertical distances.

We reviewed the different components of magnetic flux densities at the surface of the rebar, which were extracted from the optimum mesh specifications (Figure 18). The noise and out-of-range values at their minimum and results correlate well with the experimental results reported previously (Figure 19) [37]. The laboratory flux magnetic density measurements were conducted using the PMI device that was specifically developed for this work in our lab, and is on its way to being commercialized. The PMI device works through scanning the SMFL arising from ferromagnetic structures [37].

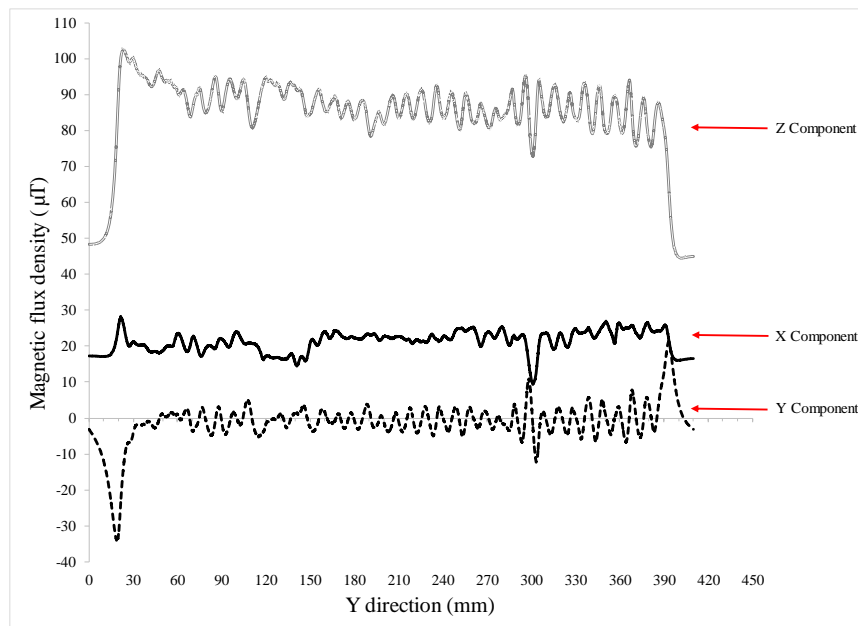


**Figure 18.** Magnetic flux density values at different axes (X, Y and Z) in the Y direction at the surface of the rebar (rebar mesh #8 and box mesh #5).

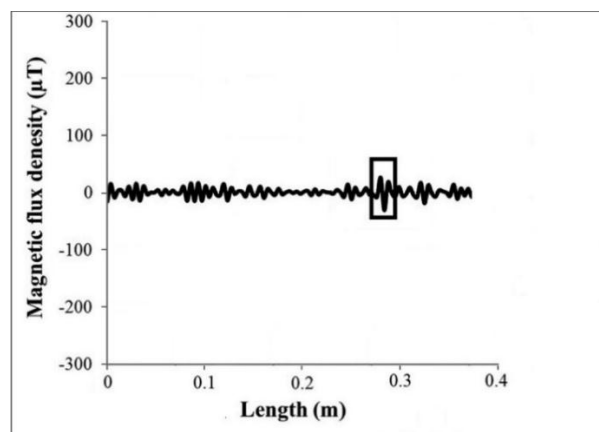


**Figure 19.** X-component of magnetic flux density resulting from the previous experiments; the square shows the Hole 2 location (modified from Mahbaz et al., 2017 [37]).

The patterns of laboratory and simulated outputs at the holes' locations follow the same trend; both curves generally have an up and down trend due to the corrugated shape of the rebar, along with a minimum value at the center of the Hole 2. As seen in Figure 18, the top hole that is ~301 mm from Edge A of the box (equal to ~282 mm from the rebar's start point (Figure 19)) is substantially easier to detect than the hole on the side of the rebar. Finding the irregularity in the magnetic data related to Hole 2 is easier because of the difference between the magnetic property of its surface (filled with air)

and the rest of the rebar’s surface (which has a different magnetic property). No detectable irregularity can be sensed in the surface magnetic flux densities for Hole 1, because more metal lies between it and the scanning line.

#### 4. Discussion

Assuming that the magnetic flux densities of different locations on the rebar are independent of one another, the probability graph method was used for fitting the magnetic flux values to a probability distribution. This method involves equating the empirical distribution of magnetic data ( $P_i$ ) with the chosen cumulative distribution function (CDF). Next, the CDF function is written in linear form, which can be expressed as Equation (10) for Gamma CDF (GAMMADIS). The linearity is then used as a basis for determining whether the data can be modeled by a particular distribution. Additionally, the goodness-of-fit of the model is given by the coefficient of determination  $R^2$ .

$$P_i = \text{GAMMADIS}(\text{magnetic data}) \rightarrow \text{magnetic data} = \text{GAMMADIS}_{\text{inverse}}(P_i) \tag{10}$$

The magnetic flux density data were plotted against various probability distributions (normal, log-normal, Weibull, and gamma distributions); a gamma distribution was chosen based on the minimum least-squared error (Figure 20). This distribution is based on a function of two parameters:  $\alpha$  and  $\beta$  (Equation (11)); these were calculated by the mean and standard deviations (SD), which are  $87.8 \mu\text{T}$  and  $25.6 \mu\text{T}$ , respectively. As observed in Figure 21, the gamma function correlates well with the histogram frequency of data, and this approximation may be useful for estimation in practical cases.

$$f(x) = \frac{1}{\beta^\alpha \Gamma(\alpha)} x^{\alpha-1} e^{-\frac{x}{\beta}} \tag{11}$$

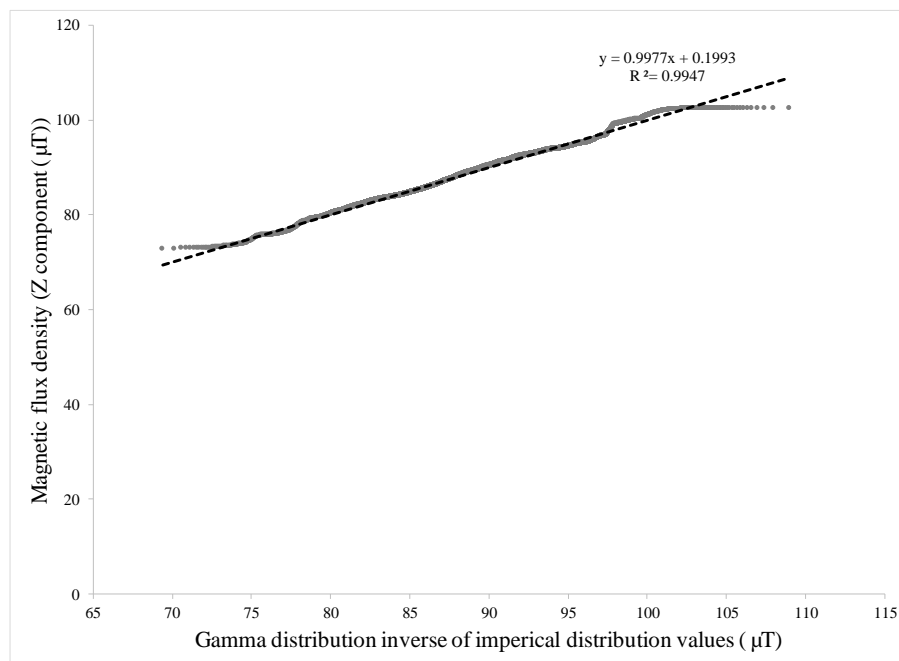


**Figure 20.** Probability plot for investigating the correlation of data with a gamma distribution.

According to Figure 18, a Z-component magnetic flux density of less than  $76 \mu\text{T}$  (without considering the edge effect and background magnetic field) corresponds to the location of Hole 2. Importing this value into the obtained CDF shows that 0.76% of the data is related to the defective locations. In other words, 0.76% of the rebar surface (at the scanned section) can be considered imperfect. This result can

be verified by the Monte Carlo simulation method (based on inverse values of the obtained gamma distribution function). Figure 22 presents the probability of defects considering the mean, SD, and limit state, showing that the probability of defectiveness fluctuates until the first 300 trials are completed, and then stabilizes at the value of ~0.75%.

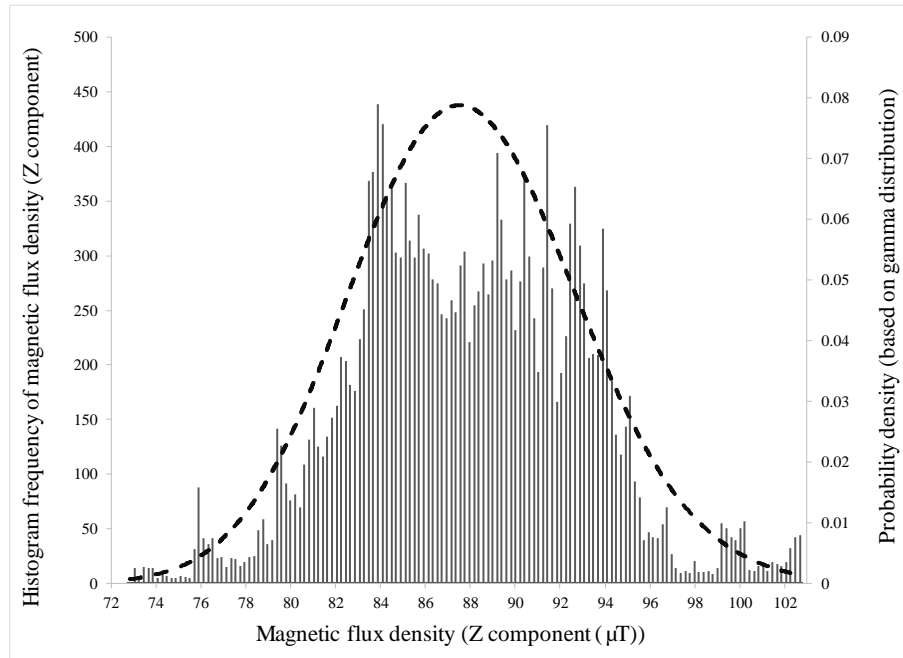


Figure 21. Histogram frequency of data in conjunction with gamma distribution probability density.

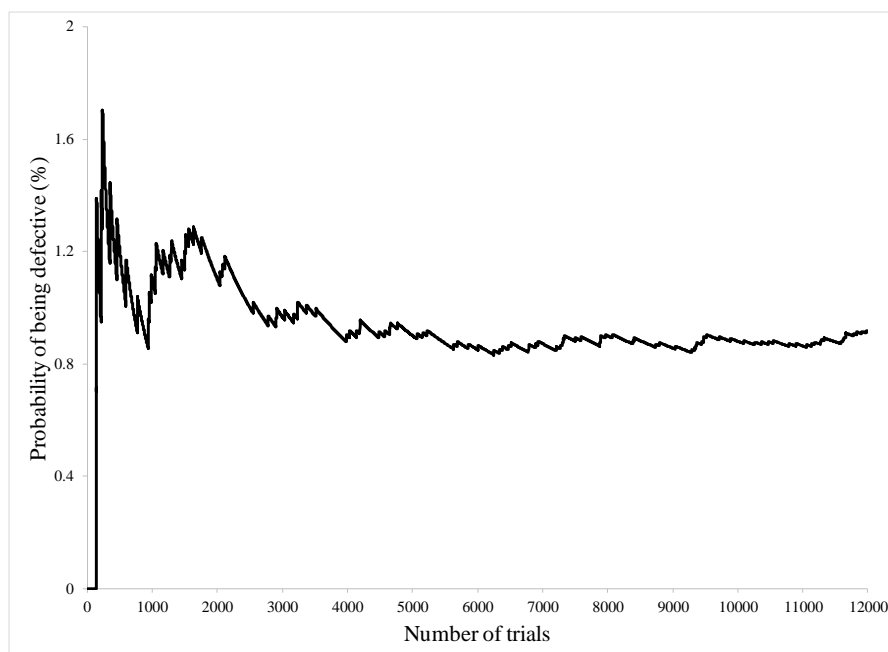


Figure 22. Defectiveness probability for the inspected rebar based on the Monte Carlo simulation method.

For our statistical investigations, we considered the magnetic data as independent variables. Those independent variables were described by the chosen probability distribution with its particular distribution parameters, knowing that distribution allowed us to estimate an interval over which the

unknown future values may lie (with a stipulated level of confidence). Using the CDF of the gamma distribution, about 98% of all of the data are from 76  $\mu\text{T}$  to 100  $\mu\text{T}$  (Equation (12)). Hence, regarding the recorded magnetic data of the rebar, it can be predicted with 98% confidence that if the rebar was longer (by how much is irrelevant), the next values indicating a flawless rebar would be somewhere between 76–100  $\mu\text{T}$ . Values outside this range should be reviewed as suspected defect locations.

$$GAMMADIS(100 \mu\text{T}) - GAMMADIS(76 \mu\text{T}) = 0.99 - 0.01 = 0.98 \quad (12)$$

Figure 23 shows the values of different components of magnetic flux densities, 16 mm from the center of the rebar. For better observation of the irregularities related to Hole 2, all of the graphs are presented from 200 mm to 370 mm at the appropriate scale. The anomaly in the magnetic values at the location of Hole 2 can be detected in all of the components of the magnetic flux densities. Figure 23 indicates that the values of the X and Y-components of magnetic flux density still include some noise that is attributable to the mesh specifications. This issue can be investigated by increasing the mesh density in both the rebar and the box containing the rebar. Additionally, increasing the quality of clouds points defining the bar geometry can help achieve more accurate outcomes. For instance, Hole 1 in the solid part produced from the captured cloud points was not as deep as the real depth (measured directly), but the mesh was not corrected, as the intent was in part to test the laser scan cloud point data without additional data input management.

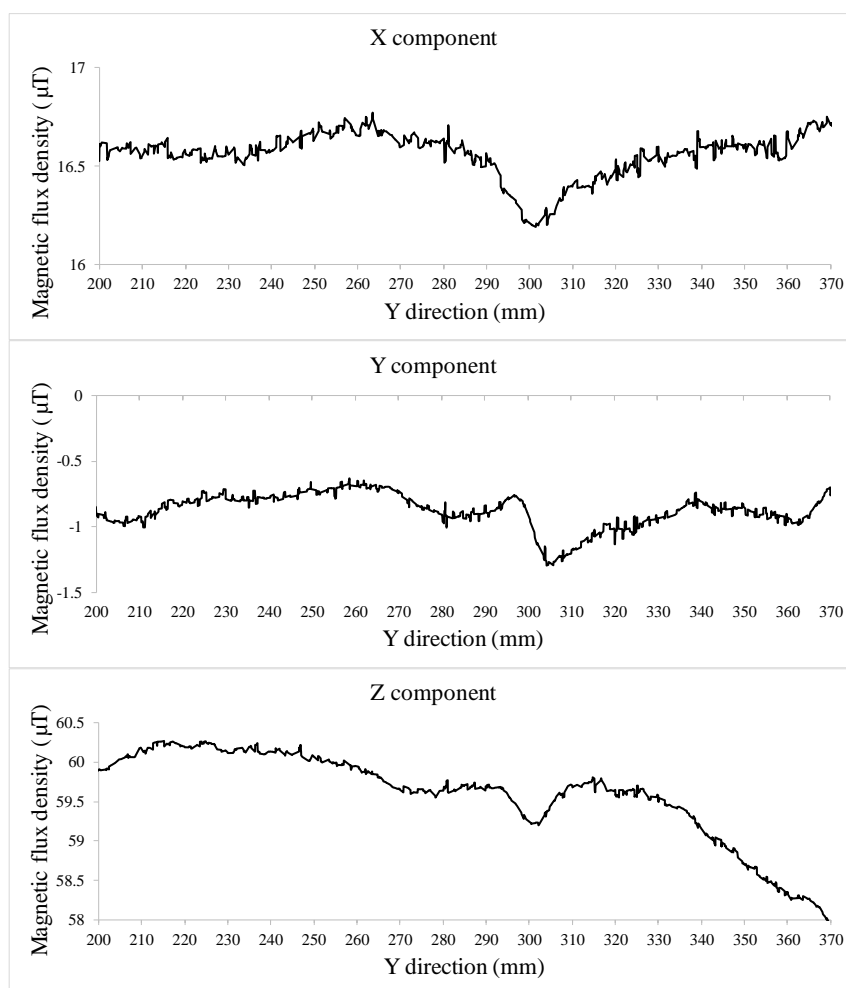


**Figure 23.** Values of different components (X, Y, and Z) of the magnetic flux densities in the Y direction, 16 mm from the center of the rebar (rebar mesh #8 and box mesh #5).

## 5. Conclusions

Being able to detect defects in steel infrastructure would substantially improve risk management and condition evaluation over time. To this end, mathematical simulations were carried out on a pre-flawed specimen that was laser-scanned to generate a point cloud surface map. This map was then used as a basis to develop a model. The intent was to establish detectability limits for very small flaws in order to reduce Type I and Type II errors in anomaly detection.

The magnetic behavior of the ferromagnetic rebar specimen was simulated with a finite element-based software considering the background magnetic field. Different components of magnetic flux densities on the surface showed consistent harmonic trends because of the corrugated shape of the rebar. However, there were specific irregularities in the direction and values for the different components of magnetic flux densities at the location of Hole 2. Simulated patterns could be correlated with the experimental data at the holes' locations, so the top hole (Hole 2) was easily located, but Hole 1 was not, because of its orientation in the magnetic field and because the point cloud model did not replicate its true depth. The gamma probability distribution was chosen to statistically assess the magnetic flux density behavior of the rebar. Two main outcomes were extracted: 0.76% of the scanned section of the rebar was considered defective, and if the rebar specimen were longer, the Z-component magnetic flux density values indicating flawless rebar would be predicted to lie between 76–100  $\mu\text{T}$  with 98% confidence.

The values of the different components of magnetic flux densities at different distances from the rebar were reviewed. Increasing the vertical distance of the data recording line led to a logarithmic reduction of magnetic flux density values. As this distance was increased, the magnetic flux density values became approximately constant and close to the background magnetic field. In conclusion:

- The pattern of the simulation results at defect locations were similar to the outputs of previous physical experiments;
- The background magnetic field had a significant effect on the trend and values of different components of the magnetic flux density;
- All of the magnetic flux density components displayed correctly located anomalies corresponding to the defect on the top surface of the rebar;
- Increasing the distance from the rebar changed the trend and values of the magnetic flux densities such that at some distance, the anomaly became undetectable;
- To detect various shapes and sizes of defects at different places along a rebar specimen, additional magnetic parameters should be considered. For instance, the Z-component of the magnetic flux density was totally constant on the sides of the rebar, and could not detect the anomaly arising from Hole 1;
- The stray magnetic field around the rebar decreased relatively symmetrically by increasing the distance from the rebar; and
- The choice of the gamma distribution to model the Z-component magnetic flux density values of the numerical simulation resulted in valuable interpretations.

**Author Contributions:** Conceptualization, M.M., S.M. and M.B.D.; Data curation, M.M. and S.M.; Formal analysis, M.M.; Funding acquisition, M.B.D.; Investigation, M.M.; Methodology, S.M.; Supervision, M.B.D.; Writing—original draft, M.M.; Writing—review & editing, M.M., S.M., and M.B.D.

**Funding:** This research received no direct funding.

**Acknowledgments:** The authors would like to thank Inspecterra Inc. for providing access to the PMI device used in this study. We would like to acknowledge CMC Microsystems for the provision of products and services that facilitated this research, including the providing of a COMSOL<sup>R</sup> software license. In addition, we express our thanks to Professor Ralph Haas and Professor Carl T. Haas for permitting us to use their laboratory (Infrastructure and sensing analysis laboratory) during our studies. we also extend our thanks to their lab member Mr. Mohammad-Mahdi Sharif due to his support for scanning the rebar by the 3D-laser scanner.

**Conflicts of Interest:** The authors declare no conflict of interest.

## References

1. Chandramauli, A.; Bahuguna, A.; Javaid, A. The analysis of plain cement concrete for future scope when mixed with glass & fibres. *IJCIET* **2018**, *9*, 230–237.
2. Hameed, R.; Sellier, A.; Turatsinze, A.; Duprat, F. Simplified approach to model steel rebar-concrete interface in reinforced concrete. *KSCE J. Civ. Eng.* **2017**, *21*, 1291–1298. [[CrossRef](#)]
3. Boyle, H.C.; Karbhari, V.M. Bond and behavior of composite reinforcing bars in concrete. *Polym. Plast. Technol. Eng.* **1995**, *34*, 697–720. [[CrossRef](#)]
4. Abouhamad, M.; Dawood, T.; Jabri, A.; Alsharqawi, M.; Zayed, T. Corrosiveness mapping of bridge decks using image-based analysis of GPR data. *Autom. Constr.* **2017**, *80*, 104–117. [[CrossRef](#)]
5. Li, F.; Ye, W. A Parameter Sensitivity Analysis of the Effect of Rebar Corrosion on the Stress Field in the Surrounding Concrete. *Adv. Mater. Sci. Eng.* **2017**, *2017*, 9858506. [[CrossRef](#)]
6. Peng, J.; Tang, H.; Zhang, J. Structural Behavior of Corroded Reinforced Concrete Beams Strengthened with Steel Plate. *J. Perform. Constr. Facil.* **2017**, *31*, 04017013. [[CrossRef](#)]
7. Desnerck, P.; Lees, J.M.; Morley, C.T. Bond behaviour of reinforcing bars in cracked concrete. *Constr. Build. Mater.* **2015**, *94*, 126–136. [[CrossRef](#)]
8. Mahbaz, S.B. Non-Destructive Passive Magnetic and Ultrasonic Inspection Methods for Condition Assessment of Reinforced Concrete. Ph.D. Thesis, Department of Civil and Environmental Engineering, University of Waterloo, Waterloo, ON, Canada, 2016.
9. Shi, Y.; Li, Z.X.; Hao, H. Bond slip modelling and its effect on numerical analysis of blast-induced responses of RC columns. *Struct. Eng. Mech.* **2009**, *32*, 251–267. [[CrossRef](#)]
10. Valipour, M.; Shekarchi, M.; Ghods, P. Comparative studies of experimental and numerical techniques in measurement of corrosion rate and time-to-corrosion-initiation of rebar in concrete in marine environments. *Cem. Concr. Compos.* **2014**, *48*, 98–107. [[CrossRef](#)]
11. Montemor, M.F.; Simões, A.M.P.; Ferreira, M.G.S. Chloride-induced corrosion on reinforcing steel: From the fundamentals to the monitoring techniques. *Cem. Concr. Compos.* **2003**, *25*, 491–502. [[CrossRef](#)]
12. Muchaidze, I.; Pommerenke, D.; Chen, G. Steel reinforcement corrosion detection with coaxial cable sensors. *Proc. SPIE Int. Soc. Opt. Eng.* **2011**, *7981*, 79811L.
13. Farhidzadeh, A.; Ebrahimkhanlou, A.; Salamone, S. A vision-based technique for damage assessment of reinforced concrete structures. *Proc. SPIE Int. Soc. Opt. Eng.* **2014**, *9064*, 90642H.
14. Takahashi, K.; Okamura, S.; Sato, M. A fundamental study of polarimetric gb-sar for nondestructive inspection of internal damage in concrete walls. *Electron. Commun. Jpn.* **2015**, *98*, 41–49. [[CrossRef](#)]
15. Concu, G.; de Nicolo, B.; Pani, L. Non-destructive testing as a tool in reinforced concrete buildings refurbishments. *Struct. Surv.* **2011**, *29*, 147–161. [[CrossRef](#)]
16. Szymanik, B.; Frankowski, P.K.; Chady, T.; Chelliah, C.R.A.J. Detection and inspection of steel bars in reinforced concrete structures using active infrared thermography with microwave excitation and eddy current sensors. *Sensors* **2016**, *16*, 234. [[CrossRef](#)] [[PubMed](#)]
17. Schneck, U. *Concrete Solutions 2014*; CRC Press: Boca Raton, FL, USA, 2014; pp. 577–585, ISBN 9781138027084.
18. Hardon, R.G.; Lambert, P.; Page, C.L. Relationship between electrochemical noise and corrosion rate of steel in salt contaminated concrete. *Br. Corros. J.* **1998**, *23*, 225–228. [[CrossRef](#)]
19. Kaur, P.; Dana, K.J.; Romero, F.A.; Gucunski, N. Automated GPR rebar analysis for robotic bridge deck evaluation. *IEEE Trans. Cybern.* **2016**, *46*, 2265–2276. [[CrossRef](#)] [[PubMed](#)]
20. Sanchez, J.; Andrade, C.; Torres, J.; Rebolledo, N.; Fulla, J. Determination of reinforced concrete durability with on-site resistivity measurements. *Mater. Struct.* **2017**, *50*, 41. [[CrossRef](#)]
21. Sabbağ, N.; Uyanık, O. Prediction of reinforced concrete strength by ultrasonic velocities. *J. Appl. Geophys.* **2017**, *141*, 13–23. [[CrossRef](#)]
22. Pei, C.; Wu, W.; Ueaska, M. Image enhancement for on-site X-ray nondestructive inspection of reinforced concrete structures. *J. X-ray Sci. Technol.* **2016**, *24*, 797–805. [[CrossRef](#)] [[PubMed](#)]
23. Hussain, A.; Akhtar, S. Review of non-destructive tests for evaluation of historic masonry and concrete structures. *Arab. J. Sci. Eng.* **2017**, *42*, 925–940. [[CrossRef](#)]
24. Xu, C.; Li, Z.; Jin, W. A new corrosion sensor to determine the start and development of embedded rebar corrosion process at coastal concrete. *Sensors* **2013**, *13*, 13258–13275. [[CrossRef](#)] [[PubMed](#)]

25. Evans, R.D.; Rahman, M. *Advances in Transportation Geotechnics 2*; CRC Press: Boca Raton, FL, USA, 2012; pp. 516–521, ISBN 9780415621359.
26. Owusu Twumasi, J.; Le, V.; Tang, Q.; Yu, T. Quantitative sensing of corroded steel rebar embedded in cement mortar specimens using ultrasonic testing. *Proc. SPIE Int. Soc. Opt. Eng.* **2016**, *9804*, 98040P.
27. Verma, S.K.; Bhadauria, S.S.; Akhtar, S. Review of nondestructive testing methods for condition monitoring of concrete structures. *Can. J. Civ. Eng.* **2013**, *2013*, 834572. [[CrossRef](#)]
28. Perin, D.; Göktepe, M. Inspection of rebars in concrete blocks. *Int. J. Appl. Electromagn. Mech.* **2012**, *38*, 65–78.
29. Makar, J.; Desnoyers, R. Magnetic field techniques for the inspection of steel under concrete cover. *NDT E Int.* **2001**, *34*, 445–456. [[CrossRef](#)]
30. Daniel, J.; Abudhahir, A.; Paulin, J. Magnetic flux leakage (MFL) based defect characterization of steam generator tubes using artificial neural networks. *J. Magn.* **2017**, *22*, 34–42. [[CrossRef](#)]
31. Wang, Z.D.; Gu, Y.; Wang, Y.S. A review of three magnetic NDT technologies. *J. Magn. Magn. Mater.* **2012**, *324*, 382–388. [[CrossRef](#)]
32. Doubov, A. Screening of weld quality using the magnetic metal memory effect. *Weld World* **1998**, *41*, 196–199.
33. Ahmad, M.I.M.; Arifin, A.; Abdullah, S.; Jusoh, W.Z.W.; Singh, S.S.K. Fatigue crack effect on magnetic flux leakage for A283 grade C steel. *Steel Compos. Struct.* **2015**, *19*, 1549–1560. [[CrossRef](#)]
34. Gontarz, S.; Maćzak, J.; Szulim, P. Online monitoring of steel constructions using passive methods. In *Engineering Asset Management—Systems, Professional Practices and Certification*; Lecture Notes in Mechanical Engineering; Springer: Cham, Switzerland, 2015; pp. 625–635.
35. Miya, K. Recent advancement of electromagnetic nondestructive inspection technology in Japan. *IEEE Trans. Magn.* **2002**, *38*, 321–326. [[CrossRef](#)]
36. Witos, M.; Zieja, M.; Zokowski, M.; Roskosz, M. Diagnosis of supporting structures of HV lines with using of the passive magnetic observer. *JSAEM Stud. Appl. Electromagn. Mech.* **2014**, *39*, 199–206.
37. Mahbaz, S.B.; Dusseault, M.B.; Cascante, G.; Vanheeghe, Ph. Detecting defects in steel reinforcement using the passive magnetic inspection method. *J. Environ. Eng. Geophys.* **2017**, *22*, 153–166. [[CrossRef](#)]
38. Hughes, D.W.; Cattaneo, F. Strong-field dynamo action in rapidly rotating convection with no inertia. *Phys. Rev. E* **2016**, *53*, 6200108. [[CrossRef](#)] [[PubMed](#)]
39. Davies, C.; Constable, C. Geomagnetic spikes on the core-mantle boundary. *Nat. Commun.* **2017**, *8*, 15593. [[CrossRef](#)] [[PubMed](#)]
40. Bezděk, A.; Sebera, J.; Klokočník, J. Validation of swarm accelerometer data by modelled nongravitational forces. *Adv. Space Res.* **2017**, *59*, 2512–2521. [[CrossRef](#)]
41. Taylor, B.K.; Johnsen, S.; Lohmann, K.J. Detection of magnetic field properties using distributed sensing: A computational neuroscience approach. *Bioinspir. Biomim.* **2017**, *12*, 036013. [[CrossRef](#)] [[PubMed](#)]
42. Zagorski, P.; Bangert, P.; Gallina, A. Identification of the orbit semi-major axis using frequency properties of onboard magnetic field measurements. *Aerosp. Sci. Technol.* **2017**, *66*, 380–391. [[CrossRef](#)]
43. Mironov, S.; Devizorova, Z.; Clergerie, A.; Buzdin, A. Magnetic mapping of defects in type-II superconductors. *Appl. Phys. Lett.* **2016**, *108*, 212602. [[CrossRef](#)]
44. Guo, L.; Shu, D.; Yin, L.; Chen, J.; Qi, X. The effect of temperature on the average volume of Barkhausen jump on Q235 carbon steel. *J. Magn. Magn. Mater.* **2016**, *407*, 262–265. [[CrossRef](#)]
45. Gupta, B.; Szielasko, K. Magnetic Sensor Principle for Susceptibility Imaging of Para- and Diamagnetic Materials. *J. Nondestruct. Eval.* **2016**, *35*, 41. [[CrossRef](#)]
46. Huang, H.; Qian, Z. Effect of temperature and stress on residual magnetic signals in ferromagnetic structural steel. *IEEE Trans. Magn.* **2017**, *53*, 6200108. [[CrossRef](#)]
47. Yuan, J.; Zhang, W. Detection of stress concentration and early plastic deformation by monitoring surface weak magnetic field change. In *Proceedings of the IEEE International Conference on Mechatronics and Automation*, Xi'an, China, 4–7 August 2010; pp. 395–400.
48. Dubov, A.A. Development of a metal magnetic memory method. *Chem. Pet. Eng.* **2012**, *47*, 837–839. [[CrossRef](#)]
49. Jarram, P. Remote measurement of stress in carbon steel pipelines—Developments in remote magnetic monitoring. In *NACE International Corrosion Conference Proceedings*; NACE International: Houston, TX, USA, 2016; pp. 1–9.
50. Tauxe, L. *Essentials of Paleomagnetism*; University of California Press: Berkeley, CA, USA, 2010; pp. 1–4, ISBN 0520260317, 9780520260313.

51. Hu, K.; Ma, Y.; Xu, J. Stable finite element methods preserving  $\nabla \cdot \mathbf{B} = 0$  exactly for MHD models. *Numer. Math.* **2017**, *135*, 371–396. [[CrossRef](#)]
52. Tabrizi, M. The nonlinear magnetic core model used in spice plus. In Proceedings of the Applied Power Electronics Conference and Exposition, San Diego, CA, USA, 2–6 March 1987; pp. 32–36.
53. Tanel, Z.; Erol, M. Students' difficulties in understanding the concepts of magnetic field strength, magnetic flux density and magnetization. *Lat.-Am. J. Phys. Educ.* **2008**, *2*, 184–191.
54. Hubert, A.; Schafer, R. *Magnetic Domains: The Analysis of Magnetic Microstructures*; Springer: Berlin/Heidelberg, Germany, 1998; pp. 109–110. ISBN 978-3-540-64108-7.
55. Kronmuller, H. Theory of nucleation fields in inhomogeneous ferromagnets. *Phys. Status Solidi B* **1987**, *144*, 385–396. [[CrossRef](#)]
56. Nahangi, M.; Haas, C. Automated 3D compliance checking in pipe spool fabrication. *Adv. Eng. Inform.* **2014**, *28*, 360–369. [[CrossRef](#)]
57. Rose, J.H.; Uzal, E.; Moulder, J.C. *Magnetic Permeability and Eddy Current Measurements*; Springer: Boston, MA, USA, 1995; Volume 14, pp. 315–322.
58. Ribichini, R. Modelling of Electromagnetic Acoustic Transducers. Ph.D. Thesis, Department of Mechanical Engineering, Imperial College, London, UK, 2011.
59. Li, Z.; Jarvis, R.; Nagy, P.B.; Dixon, S.; Cawley, P. Experimental and simulation methods to study the Magnetic Tomography Method (MTM) for pipe defect detection. *NDT E Int.* **2017**, *92*, 59–66. [[CrossRef](#)]



© 2018 by the authors. Licensee MDPI, Basel, Switzerland. This article is an open access article distributed under the terms and conditions of the Creative Commons Attribution (CC BY) license (<http://creativecommons.org/licenses/by/4.0/>).